Scientific Research Publishing

Advances in Materials Physics and Chemistry, 2026, 16(2), 69-85
https://www.scirp.org/journal/ampc
ISSN Online: 2162-5328
ISSN Print: 2162-531X

Numerical Investigation of Performance in $MAPI_{1-x}Cl_x$ Perovskite Solar Cells Employing Hybrid Electron Transport Layers

Boureima Traore, Valentin Tapsoba, Adama Zongo, Soumaila Ouedraogo, Issiaka Sankara, Francois Zougmore

Département de Physique, Laboratoire de Matériaux et Environnement (LA.M.E)-UFR/SEA, Université Joseph Ki-Zerbo, Ouagadougou, Burkina Faso
Email: traoreboureim@gmail.com, valpero2018@gmail.com, zongadamss@gmail.com, ouedraogosoumaila1@gmail.com, sankaraissaka@gmail.com, zougfran2013@gmail.com

How to cite this paper: Traore, B., Tapsoba, V., Zongo, A., Ouedraogo, S., Sankara, I. and Zougmore, F. (2026) Numerical Investigation of Performance in $MAPI_{1-x}Cl_x$ Perovskite Solar Cells Employing Hybrid Electron Transport Layers. *Advances in Materials Physics and Chemistry*, **16**, 69-85.
https://doi.org/10.4236/ampc.2026.162004

Received: January 4, 2026
Accepted: January 30, 2026
Published: February 2, 2026

Abstract

In this work, a numerical study was carried out to analyze the impact of hybrid electron transport layers (h-ETLs) on the performance of $MAPI_{1-x}Cl_x$ perovskite solar cells (PSCs) using the SCAPS-1D simulation software. Various h-ETL architectures, including PCBM-SnS_2, TiO_2-SnO_2, PCBM/PCPB, and TiO_2/ZnO, were investigated in order to optimize charge extraction and reduce recombination losses. The results indicate that the TiO_2-SnO_2 configuration exhibits the best optoelectronic performance, owing to favorable energy band alignment and enhanced electron transport properties. Parametric analysis reveals that an optimal absorber thickness of approximately 450 nm and an h-ETL thickness of about 30 nm lead to maximum power conversion efficiency. Furthermore, the investigation of defect density effects highlights that device performance is strongly dependent on defect states within the absorber layer, with defect densities below 10^{15} cm^{-3} resulting in significant improvements in short-circuit current density, open-circuit voltage, and overall efficiency. These findings emphasize the critical role of defect control in the development of high-efficiency and improved-stability perovskite solar cells.

Keywords

$MAPI_{1-x}Cl_x$ Perovskite, Hybrid ETL, Numerical Simulation, SCAPS-1D

1. Introduction

Over the past decade, hybrid halide perovskite solar cells (PSCs) have attracted significant attention in the photovoltaic community owing to their outstanding

optoelectronic properties and low-cost fabrication potential. These materials exhibit a high absorption coefficient, excellent charge carrier mobility, long carrier diffusion lengths, and a tunable bandgap, making them particularly attractive for photovoltaic applications [1]-[3]. As a result of these advantages, the power conversion efficiency (PCE) of perovskite solar cells has rapidly increased from 3.8% in 2009 to over 26% today, rivaling conventional photovoltaic technologies [4]. Among the various perovskite compositions investigated, methylammonium lead iodide ($CH_3NH_3PbI_3$ or MAPI) has been widely used as a model absorber material due to its simple crystal structure, ease of synthesis, and favorable photovoltaic performance [5]. However, devices based on pristine MAPI still suffer from significant limitations, including thermal and environmental instability, moisture-induced degradation, and enhanced non-radiative recombination caused by crystal defects and trap states at grain boundaries [6] [7]. To overcome these limitations, several strategies have been proposed, among which partial halide substitution has proven particularly effective. The incorporation of chlorine into the perovskite lattice, leading to the $MAPI_{1-x}Cl_x$ composition, has been shown to significantly improve film morphology, crystallinity, charge carrier mobility, and diffusion length [8] [9]. Although the actual amount of chlorine incorporated into the perovskite lattice is often small, its role in crystallization kinetics and defect passivation is now well established [10] [11]. These improvements translate into enhanced short-circuit current density (J_{SC}), open-circuit voltage (V_{OC}), and overall device stability. Beyond the absorber layer, the electron transport layer (ETL) plays a crucial role in the architecture of perovskite solar cells by ensuring efficient extraction of photogenerated electrons while blocking hole transport, thereby reducing interfacial recombination losses [12]. Conventional ETL materials such as TiO_2, SnO_2, and ZnO have enabled high-efficiency devices; however, they still present several drawbacks, including high processing temperatures, ultraviolet light instability, and high surface defect densities, which may limit device performance and long-term stability [13] [14]. In this context, the development of alternative electron transport layers has become a major research focus. Hydride electron transport layers (h-ETLs) have emerged as promising candidates due to their wide bandgaps, good electronic conductivity, low trap-state density, and compatibility with low-temperature fabrication processes [15] [16]. Moreover, some hydride layers exhibit high chemical and thermal stability, which can further enhance the durability of perovskite solar cells [17]. The integration of h-ETLs into $MAPI_{1-x}Cl_x$-based devices could therefore provide improved energy level alignment, promote more efficient electron extraction, reduce interfacial recombination losses, and enhance both photovoltaic performance and device stability. Nevertheless, studies specifically addressing the combination of chlorinated perovskites with hydride transport layers remain limited, and the physical mechanisms governing the h-ETL/$MAPI_{1-x}Cl_x$ interface are not yet fully understood. In this work, we present a comprehensive numerical investigation of $MAPI_{1-x}Cl_x$ perovskite solar cells incorporating a hydride electron transport layer (h-ETL). The objective is to analyze the

influence of the h-ETL on the structural, optical, and electronic properties of the device, as well as on its photovoltaic performance and stability.

2. Device Model and Simulation Details

The solar cells investigated in this work are based on a planar n-i-p architecture with the following structure: FTO/h-ETL/$MAPI_{1-x}Cl_x$/HTL/Au, as illustrated in Figure 1. The schematic energy band alignment of the different materials used in this perovskite solar cell is also shown in Figure 1.

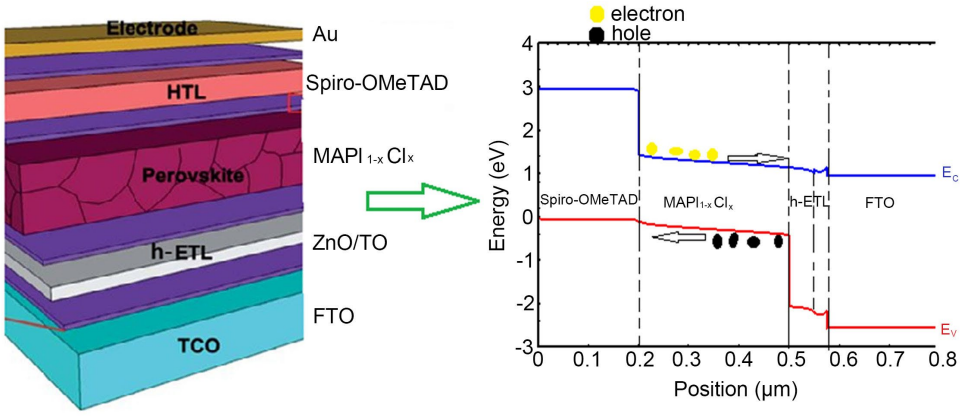

Figure 1. Modeled structure of a solar cell based on $MAPI_{1-x}Cl_x$ and energy band diagram.

This device architecture is widely adopted for the investigation of interfacial effects in high-efficiency perovskite solar cells [1] [3] [12].

In this configuration, fluorine-doped tin oxide (FTO)-coated glass is employed as the transparent front electrode, ensuring high optical transmittance and good electrical conductivity. The FTO layer serves as the electron-collecting contact, enabling efficient extraction of electrons from the electron transport layer. A hybrid electron transport layer (h-ETL) is deposited onto the FTO substrate and acts as a selective contact for electrons, facilitating their extraction while blocking holes, thereby reducing recombination losses at the h-ETL/$MAPI_{1-x}Cl_x$ interface. The wide bandgap of the h-ETL and its favorable energy alignment with the conduction band of the perovskite absorber contribute to minimizing both optical and electrical losses [13] [14] [17]. The $MAPI_{1-x}Cl_x$ ($CH_3NH_3PbI_{3-x}Cl_x$) absorber layer is deposited on top of the h-ETL and constitutes the active region of the solar cell, where photon absorption and electron-hole pair generation occur. Although the chemical composition of the material is not explicitly defined in SCAPS-1D, the physical effects of chlorine are effectively captured through a set of electronic parameters. Chlorine incorporation enhances carrier lifetime by reducing the bulk defect density (N_t) in the absorber layer. It is well established that the presence of chlorine promotes improved crystallinity and passivation of deep-level defects, which is numerically reflected by a reduction in Shockley-Read-Hall (SRH) recombination rates. A hole transport layer (HTL) is subsequently introduced to ensure efficient extraction of photogenerated holes toward the back electrode. In

perovskite solar cells, materials such as PEDOT:PSS, Spiro-OMeTAD, and more recently CBTS (Cu_2BaSnS_4) are commonly employed as HTLs due to their good processability, favorable energy level alignment with perovskites, and efficient hole transport properties [18]. Numerical simulation and device modeling play a crucial role in identifying suitable materials for the various layers of perovskite solar cells, as the experimental fabrication of multilayer perovskite devices is both time-consuming and costly [19]. In this work, the photovoltaic performance of the devices is investigated using the SCAPS-1D (Solar Cell Capacitance Simulator) software, developed at the University of Ghent by Marc Burgelman. SCAPS-1D is based on the numerical solution of Poisson's equation and the carrier continuity equations [20], as described by Equation (1) and Equation (2).

$$\operatorname{div}\left(-\operatorname{grad}\psi\right)=\frac{q}{\varepsilon}\left[p\left(x\right)-n\left(x\right)+N_D^+\left(x\right)-N_A^-\left(x\right)\right] \tag{1}$$

$$\nabla J_n=q\left[R\left(x\right)-G\left(x\right)\right]+q\frac{\partial n}{\partial t} \tag{2}$$

$$\nabla J_p=q\left[G\left(x\right)-R\left(x\right)\right]+q\frac{\partial p}{\partial t} \tag{3}$$

Equation (1) describes the phenomena of electrostatic nature, where ψ is the electrostatic potential; n and p are the densities of free electrons and holes, respectively; and $N_D^+\left(x\right)$ and $N_A^-\left(x\right)$ are the concentrations of ionized donor and acceptor, respectively. Equation (2) and Equation (3) govern the dynamic equilibrium condition in a semiconductor, where G is the generation rate; Rn and Rp are the recombination rates of electrons and holes, respectively; and Jn and Jp are the current densities of electrons and holes, respectively; their terms are found in literature. The physical properties of the different layers used in the numerical simulations are summarized in Table 1.

Table 1. SCAPS-1D input parameters of the materials used in the simulation.

	FTO	ZnO	TiO_2	$MAPI_{1-x}Cl_x$	Spiro-OMeTAD
Thickness (nm)	0.27	0.015	0.04	0.333	0.15
Band gap (eV)	3.5	3.3	3.2	1.55	3
Electron Affinity (eV)	4.7	4.3	4.2	3.9	2.45
Dielectric relative Permittivity	9	9	9	6.5	3
Effective density of state in BC (cm^{-3})	2.2×10^{18}	2.2×10^{18}	10^{19}	2.2×10^{18}	10^{19}
Effective density of state in BV (cm^{-3})	1.8×10^{19}	1.8×10^{19}	10^{19}	1.8×10^{19}	10^{19}
Electrons thermal velocity (cm/s)	10^7	10^7	10^7	10^7	10^7
Holes thermal velocity (cm/s)	10^7	10^7	10^7	10^7	10^7
Electrons Mobility (cm^2/Vs)	33	50	20	2	10^{-4}
Holes Mobility (cm^2/Vs)	8	25	1	2	10^{-4}
Donor density N_D (cm^{-3})	10^{18}	10^{18}	10^{17}	-	-
Acceptor density N_A (cm^{-3})	-	-	-	10^{15}	2×10^{18}

Continued

Bulk defect properties				
Bulk defect Density (cm^{-3})	10^{17}	10^{17}	10^{15}	10^{15}
Capture cross-section electrons (cm^2)	10^{-19}	10^{-19}	10^{-19}	10^{-14}
Capture cross-section holes (cm^2)	10^{-19}	10^{-19}	10^{-19}	2×10^{-14}

These parameters were adopted from previously reported theoretical and experimental studies by Kanoun *et al.*, MallaHasan *et al.*, Targhi *et al.*, and Sharma *et al.* [21]-[24]. All simulations were performed under standard illumination conditions using an incident power density of 1000 $W \cdot m^{-2}$, a cell temperature maintained at 300 K, and the AM 1.5 G solar spectrum, accounting for both direct and diffuse solar radiation.

3. Result and Discussion

3.1. Influence of Different Hybrid Electron Transport Layer (h-ETL) Materials on the Performance of Perovskite Solar Cells

The electron transport layer (ETL) plays a fundamental role in the operation of perovskite solar cells (PSCs). It ensures efficient extraction of photogenerated electrons from the absorber layer toward the collecting electrode, while simultaneously acting as a selective barrier for holes, thereby limiting interfacial recombination losses [1]. Moreover, the electronic and structural properties of the ETL directly influence charge transport, interfacial energy level alignment, and the overall stability of the device [3].

In conventional perovskite solar cell architectures, titanium dioxide (TiO_2) is widely employed as the ETL material owing to its chemical stability and suitable energy alignment with perovskite absorbers. However, TiO_2 suffers from several limitations, including relatively low electron mobility, a high density of surface trap states, and photochemical instability under ultraviolet irradiation, which can lead to gradual degradation of device performance [12] [13]. These drawbacks have motivated the search for alternative materials or hybrid structures capable of enhancing electron transport while suppressing recombination processes. In this context, the introduction of hybrid electron transport layers (h-ETLs), combining inorganic and organic materials, has emerged as a promising strategy. Materials such as PCBM (6,6-phenyl-C_{61}-butyric acid methyl ester), SnS_2, ZnO, and SnO_2 have been extensively investigated as ETL components due to their high electron mobility, favorable band alignment with perovskite absorbers, and ability to passivate interfacial defects. In particular, hybrid architectures such as PCBM/SnS_2, TiO_2/ZnO, TiO_2/SnO_2, and PCBM/PCPB allow the advantages of each constituent material to be combined, leading to improved electron extraction, reduced interfacial recombination, and enhanced operational stability [16] [23]. In this work, these hybrid materials are investigated as potential alternatives to conventional TiO_2-based ETLs. The physical parame-

ters associated with each h-ETL, including electron mobility, electron affinity, bandgap, and defect density, are carefully considered to evaluate their impact on the overall device performance. The ETL thickness is fixed at 50 nm in order to isolate the effect of intrinsic material properties on charge transport and photovoltaic parameters, enabling a consistent and meaningful comparison among the different configurations studied. The properties of the various h-ETL layers were adopted from previously reported theoretical and experimental studies [25]-[27]. The hybrid ETLs presented in **Table 2** were not directly measured in this study but were derived from the existing literature using a combined approach that is widely adopted in numerical simulations of perovskite solar cells. The h-ETL parameters were directly extracted from experimental or theoretical values reported in the literature (Refs. Patil *et al.*, Li *et al.*, Hossain *et al.*). The physical parameters of the h-ETLs listed in **Table 2** therefore correspond to a combination of literature-based experimental values, effective medium approximations, and numerical calibration consistent with the reported experimental device performances.

Table 2. Parameters for different hybrid electron transport layer.

	PCBM-SnS_2	TiO_2-SnO_2	PCBM-PCPB
Thickness (nm)	50	50	50
Band gap (eV)	1.57	3.3	2
Electron Affinity (eV)	4	4	3.9
Dielectric relative Permittivity	4.2	9	3.9
Effective density of state in BC (cm^{-3})	2.5×10^{19}	2.1×10^{18}	2.5×10^{21}
Effective density of state in BV (cm^{-3})	2.5×10^{19}	1.8×10^{19}	2.5×10^{21}
Electrons thermal velocity (cm/s)	10^7	10^7	10^7
Holes thermal velocity (cm/s)	10^7	10^7	10^7
Electrons Mobility (cm^2/Vs)	2.89×10^{-1}	30	30
Holes Mobility (cm^2/Vs)	2.89×10^{-1}	15	15
Bulk defect properties			
Bulk defect Density (cm^{-3})	10^{15}	10^{15}	10^{15}
Capture cross-section electrons (cm^2)	2×10^{-14}	2×10^{-14}	10^{-14}
Capture cross-section holes (cm^2)	2×10^{-14}	2×10^{-14}	2×10^{-14}

Figure 2 and **Figure 3** present the J-V characteristics and external quantum efficiency (EQE) spectra, respectively, corresponding to different h-ETL materials.

To facilitate a detailed analysis of the J-V behavior, the key photovoltaic parameters extracted from the J-V curves for the different h-ETL configurations are summarized in **Table 3**.

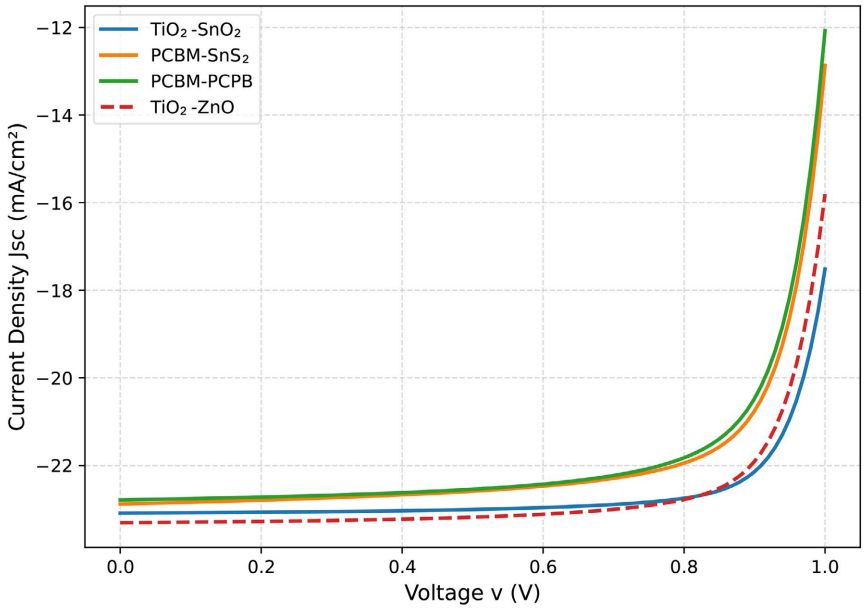

Figure 2. Effect of different h-ETL materials on J-V characteristics and (b) quantum efficiency of a $MAPI_{1-x}Cl_x$-based solar cell.

Table 3. Parameters for different hybrid electron transport layer used in the numerical simulation.

	$\eta(\%)$	FF(%)	$V_{OC}(V)$	$J_{SC}\left(mA/cm^2\right)$
TiO_2-SnO_2	20.062	73.671	1.179	23.085
PCBM-SnS_2	18.681	75.592	1.080	22.880
PCBM-PCPB	18.444	75.522	1.071	22.786
TiO_2-ZnO	19.739	75.085	1.128	23.305

Table 3 indicates that the solar cell exhibits a relatively low power conversion efficiency when PCBM-PCPB is employed as the h-ETL, whereas a high efficiency of 20.062% is achieved with TiO_2-SnO_2 as the hybrid electron transport layer. The TiO_2-ZnO-based device also demonstrates notable performance, with a conversion efficiency of 19.739%.

Figure 3 illustrates the evolution of the external quantum efficiency as a function of wavelength for the different h-ETL configurations, namely TiO_2-SnO_2, PCBM-SnS_2, PCBM-PCPB, and TiO_2-ZnO. These EQE curves provide essential insights into the ability of the devices to convert incident photons into photogenerated charge carriers. In the UV-blue region, noticeable differences are observed among the studied architectures. Devices incorporating PCBM-based hybrid layers (PCBM-SnS_2 and PCBM-PCPB) exhibit a slightly lower response compared to purely inorganic structures (TiO_2-SnO_2 and TiO_2-ZnO). In the visible wavelength range (400 - 750 nm), where $MAPI_{1-x}Cl_x$ exhibits strong absorption, all configurations show high EQE values exceeding 85%, indicating efficient light absorption and effective carrier transport.

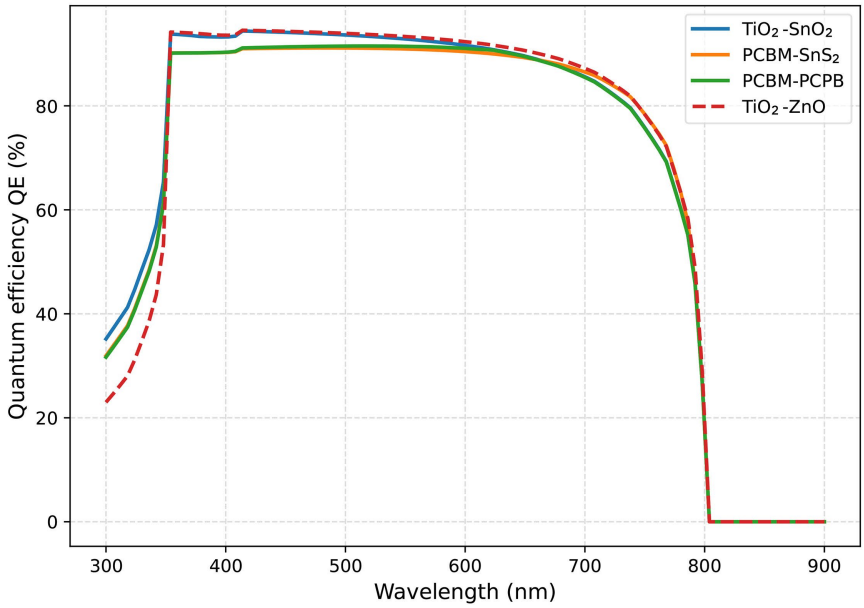

Figure 3. Effect of different h-ETL materials on quantum efficiency of a $MAPI_{1-x}Cl_x$-based solar cell.

At longer wavelengths (>750 nm), a sharp decrease in EQE is observed beyond 780 - 800 nm, corresponding to the absorption edge of the $MAPI_{1-x}Cl_x$ perovskite absorber, in agreement with its bandgap energy (~1.55 - 1.60 eV). Overall, the PCBM-SnS_2 and TiO_2-SnO_2-based architectures exhibit the best spectral performance, reflecting more efficient electron extraction and reduced recombination losses. These results are in good agreement with previous studies reported by Yang *et al.* [26], who demonstrated that PCBM-SnS_2-based ETLs significantly enhance electron extraction and spectral response in perovskite solar cells. The observed performance enhancement can be attributed primarily to improved energy level alignment between the conduction band of the perovskite absorber and that of the h-ETL. Based on these findings, TiO_2-SnO_2 is selected as the hybrid electron transport layer for the remainder of this study, as it enables the highest power conversion efficiency of 20.062%, an open-circuit voltage V_{OC} of 1.179 V, a short-circuit current density J_{SC} of 23.085 mA·cm^{-2}, and a fill factor of 73.671% were obtained. These values are in good agreement with those reported for experimental planar perovskite solar cells in the literature. Green *et al.* showed that organometal halide perovskite solar cells based on $CH_3NH_3PbI_3$ typically exhibit V_{OC} values ranging from 1.05 to 1.20 V and current densities exceeding 22 mA·cm^{-2}, closely matching the simulated results of this study [2]. Similarly, You *et al.* reported planar heterojunction perovskite solar cells with J_{SC} values in the range of 22 - 24 mA·cm^{-2} and efficiencies around 20%, confirming that the simulated performance levels are representative of real devices [21]. The results of Chen *et al.* on planar cells fabricated via a vapor-assisted process also show comparable electrical parameters, particularly in terms of efficiency and current density [10].

3.2. Influence of the Hybrid Electron Transport Layer (h-ETL) and Absorber Thickness

In this section, the combined influence of the hybrid electron transport layer (h-ETL) thickness and the absorber thickness is investigated. The h-ETL selected for this study is **TiO_2-SnO_2**, while the absorber layer consists of **$MAPI_{1-x}Cl_x$**. The thickness of the h-ETL is varied from **10 nm to 100 nm**, whereas the absorber thickness ranges from **100 nm to 1000 nm**, as illustrated in the corresponding Figure 4.

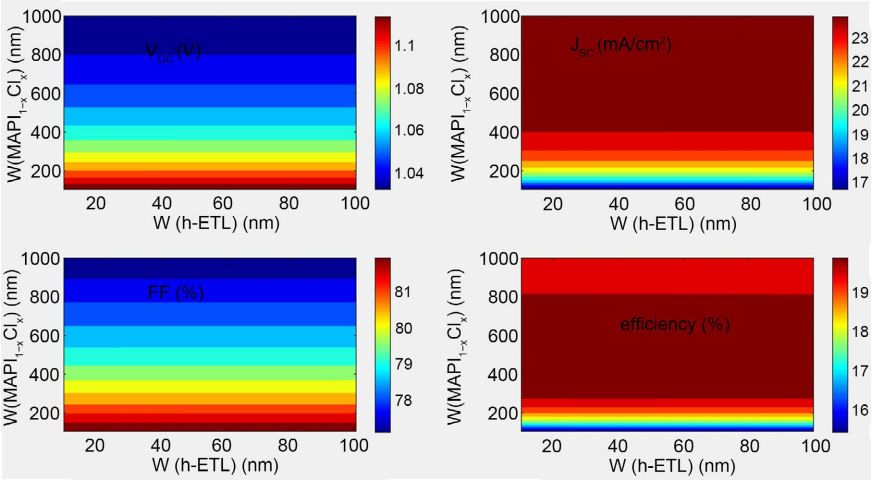

Figure 4. The influence of the $MAPI_{1-x}Cl_x$ absorber thickness on the electrical parameters as a function of the h-ETL thickness.

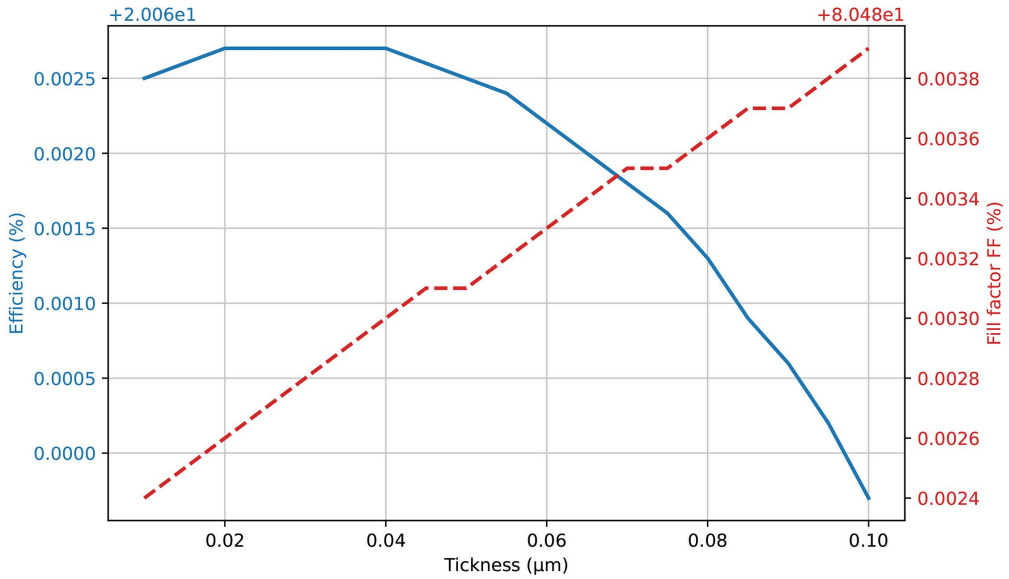

Figure 5. Influence of the h-ETL thickness on the fill factor and conversion efficiency.

In general, variations in both layer thicknesses lead to changes in all electrical parameters, although the h-ETL thickness exhibits a comparatively weaker influence. An excessively thin h-ETL may not fully cover the substrate, resulting in

increased interfacial recombination and defect formation, while an overly thick h-ETL increases the series resistance of the device. To determine the optimal h-ETL thickness, the electrical parameters of the perovskite solar cell (PSC) were plotted as a function of the h-ETL thickness, as shown in Figure 5 and Figure 6.

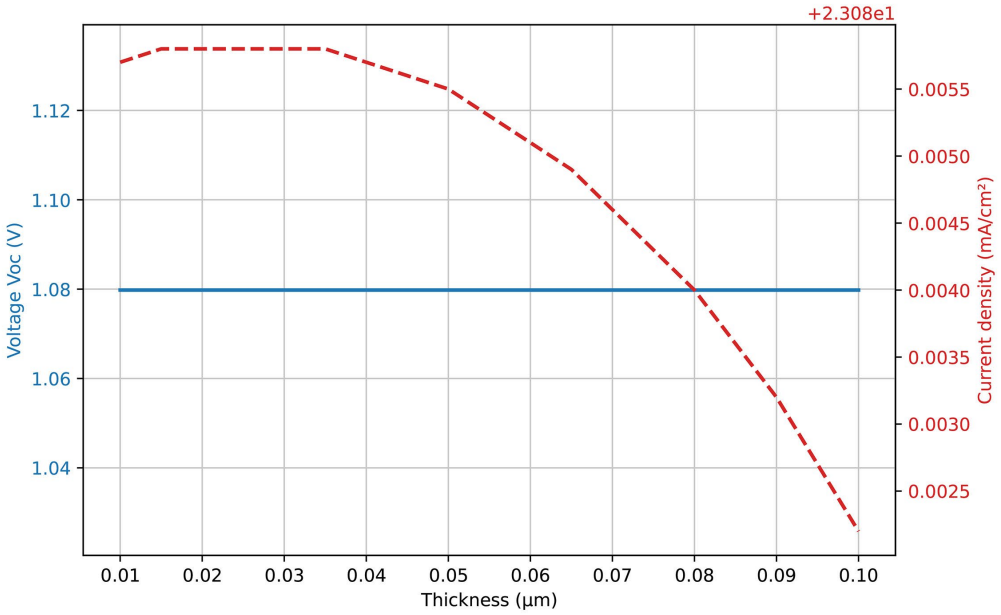

Figure 6. Influence of the h-ETL thickness on the open-circuit voltage and short-circuit current density.

The results indicate that optimal device performance is achieved for an h-ETL thickness of approximately **30 nm**. Regarding the absorber thickness, the $MAPI_{1-x}Cl_x$ layer has a significant impact on all electrical parameters. The open-circuit voltage V_{OC} and the fill factor (FF) exhibit similar trends, both decreasing as the absorber thickness increases. In contrast, the short-circuit current density J_{SC} increases with absorber thickness, reflecting enhanced photon absorption. The power conversion efficiency decreases sharply when the absorber thickness is below **300 nm** or exceeds **800 nm**, indicating that optimal PSC performance is achieved for absorber thicknesses in the range of **300 - 800 nm**.

These trends can be attributed to a balance between maximal optical absorption, reduced recombination losses, and efficient electron transport through the h-ETL. The obtained results are consistent with previous studies by Green *et al.* [2], who reported that absorber thicknesses in the range of **400 - 500 nm** are often optimal for planar PSC architectures. Such thicknesses enable efficient visible light harvesting while maintaining fast charge transport toward the contacts, thereby minimizing recombination losses and internal resistances. For thicker perovskite layers, carrier transport limitations become more pronounced. Although mixed-halide perovskites such as $MAPI_{1-x}Cl_x$ exhibit longer carrier diffusion lengths exceeding **1 μm** compared to pure iodide perovskites [8], absorber thicknesses below **600 nm** are generally recommended to limit recombination effects. Based on the above analysis, the h-ETL thickness has a relatively weak influence on the electri-

cal parameters, whereas absorber thicknesses between **300 nm and 800 nm** yield optimal device performance.

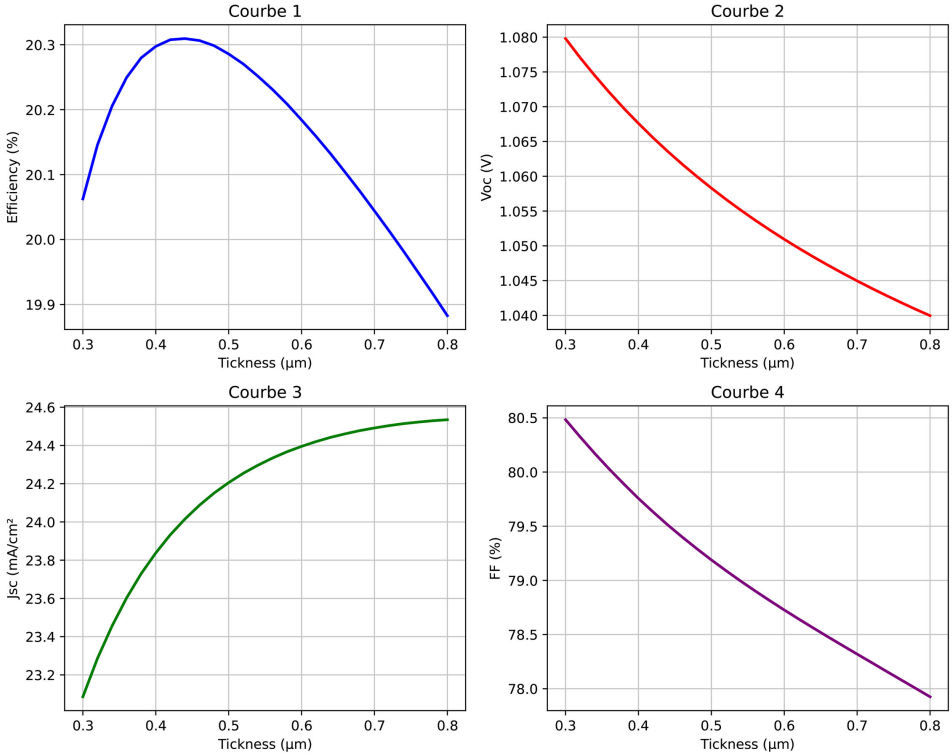

Figure 7. Influence of the absorber thickness on electric parameters.

To further refine the absorber thickness optimization, a detailed analysis of absorber thicknesses within this range was performed, as shown in **Figure 7**, which presents the dependence of J_{SC}, V_{OC}, FF and η on the $MAPI_{1-x}Cl_x$ thickness. As observed in **Figure 7**, the power conversion efficiency increases with absorber thickness and reaches a maximum value of **20.37%** at an absorber thickness of approximately **450 nm**, beyond which the efficiency decreases. Both V_{OC}, and FF exhibit decreasing trends with increasing absorber thickness, while J_{SC} continuously increases, indicating improved conversion of absorbed photons into photogenerated carriers.

Overall, this study demonstrates that optimal PSC performance is achieved with an absorber thickness of approximately 450 nm and an h-ETL thickness of about 30 nm. The corresponding electrical parameters are summarized in **Table 4**, which compares the performance of the standard and optimized PSC configurations.

Table 4. The performance of the standard and optimized PSC configurations.

	$\eta(\%)$	$FF(\%)$	$V_{OC}(V)$	$J_{SC}(mA/cm^2)$
PCS standard	20.062	73.671	1.179	23.085
PCS optimized	20.309	75.988	1.111	24.053
Relative improvement	1.23%	+3.15%	−5.77%	+4.19%

The optimized perovskite solar cell exhibits a significant increase in J_{SC} of +4.19%, which can be attributed to enhanced optical absorption and more efficient electron collection and transport through the h-ETL. A slight decrease in V_{OC} of −5.77% is observed, while the fill factor increases significantly by +3.15%. This decrease in V_{OC} can be attributed to unfavorable conduction band alignment at the interface between the h-ETL and the $MAPI_{1-x}Cl_x$ absorber. In this case, the simultaneous increase in J_{SC} and the fill factor (FF) largely compensates for the loss in V_{OC}, resulting in an overall improvement in power conversion efficiency. The optimized perovskite solar cell is therefore more efficient, although slightly more prone to recombination. Despite the reduction in V_{OC} the optimized PSC achieves a higher power conversion efficiency of 20.309%, compared to 20.062% for the standard device, corresponding to a relative improvement of 1.23%. These results indicate that the proposed optimization strategy is both effective and physically consistent, particularly for applications targeting enhanced current density and fill factor rather than voltage gains.

3.3. Influence of Defect Density in the Hybrid Electron Transport Layer (h-ETL) and the Absorber

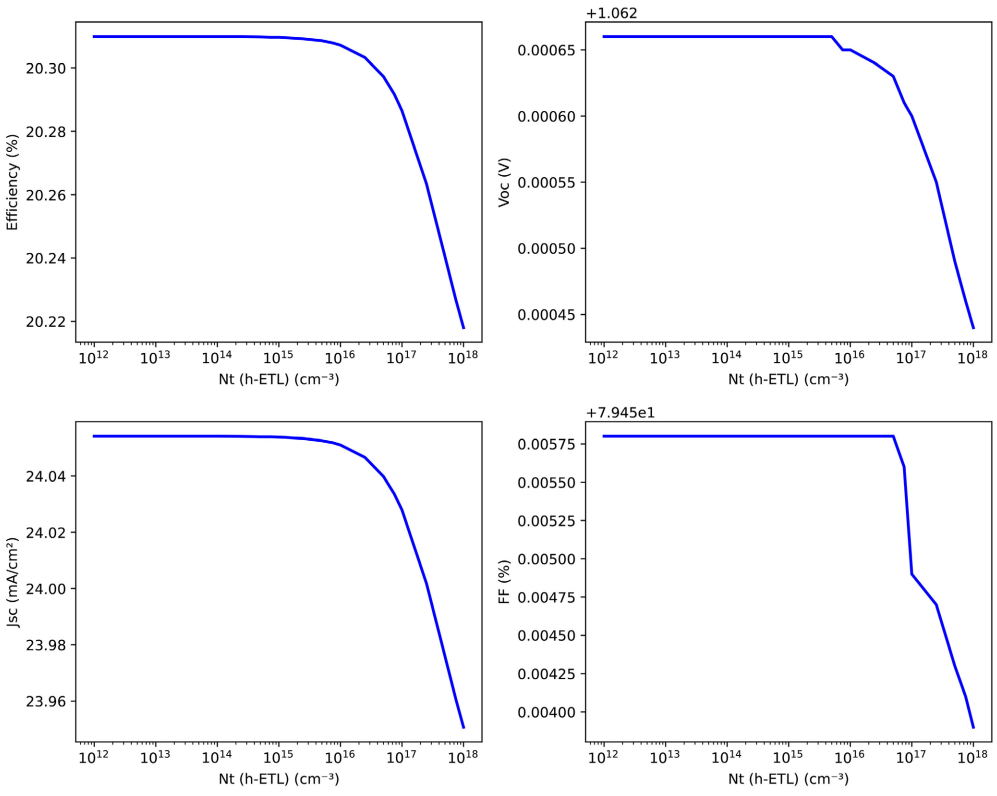

Figure 8. Influence of the defect density N_t in the h-ETL on the electrical parameters.

In perovskite solar cells, interfacial recombination particularly at the h-ETL/absorber interface can constitute a dominant loss mechanism. In the present study, the simulation was deliberately focused on bulk defects within the absorber layer

in order to systematically isolate and analyze the impact of the intrinsic material parameters and the h-ETL on device performance. This choice is justified by the fact that the h-ETLs are designed to improve interfacial quality, reduce energy band mismatches, and provide effective passivation of interfacial defect states. Figure 8 illustrates the influence of the defect density N_t in the hybrid electron transport layer (h-ETL) on the electrical parameters of the perovskite solar cell (PSC). This analysis allows the identification of three distinct regimes. For Pour $N_t \leq 10^{15}$ cm^{-3}, very good device performance is obtained, with all electrical parameters remaining nearly unchanged. This behavior can be attributed to negligible carrier recombination resulting from the low density of defects. In the intermediate range, $10^{15} < N_t \leq 10^{17}$ cm^{-3}, a gradual decrease in all electrical parameters is observed. When the defect density exceeds $10^{17} < N_t \leq 10^{18}$ cm^{-3}, a drastic degradation of all PSC parameters occurs, which can be ascribed to enhanced recombination processes mediated by the high density of defect states. Overall, the performance of $MAPI_{1-x}Cl_x$-based solar cells remains weakly sensitive to the defect density of the h-ETL as long as it remains below approximately 10^{15} cm^{-3}. Beyond this critical threshold, recombination becomes dominant, leading to a rapid decline in all electrical parameters. The defect density N_t within the $MAPI_{1-x}Cl_x$ absorber bulk is a crucial parameter governing the performance and stability of perovskite solar cells. It is generally reported to lie in the range from 10^{13} cm^{-3} to 10^{18} cm^{-3} [26]. In this study, the impact of defect density in the $MAPI_{1-x}Cl_x$ absorber layer on the electrical performance and stability of PSCs is analyzed, as shown in Figure 9. In general, all electrical parameters $(J_{SC}, V_{OC}, FF, \eta)$ decrease with increasing defect density in the $MAPI_{1-x}Cl_x$ absorber. The performance of $MAPI_{1-x}Cl_x$-based solar cells remains nearly unchanged as long as the absorber defect density is below 10^{13} cm^{-3}, with a power conversion efficiency exceeding 22.25%, an open-circuit voltage close to 1.24 V, a short-circuit current density of approximately 24 mA·cm^{-2}, and a fill factor above 80%. These excellent performances can be attributed to negligible non-radiative recombination and nearly optimal charge carrier collection. Beyond this critical value, a progressive degradation of device performance is observed due to the dominance of non-radiative recombination, resulting in a pronounced reduction of the short-circuit current density J_{SC}. These findings are consistent with the works of Tress *et al.* [22] and Stranks *et al.* [8], who also reported a gradual decrease in J_{SC} when the defect density exceeds 10^{15} cm^{-3}. Above this threshold, the fill factor (FF), power conversion efficiency (η), and open-circuit voltage V_{OC} decrease almost linearly with increasing defect density. These results confirm that the performance of $MAPI_{1-x}Cl_x$ perovskite solar cells is extremely sensitive to the crystalline quality of the absorber layer and that controlling the defect density below approximately 10^{15} cm^{-3} is a key requirement for achieving high efficiency and long-term stability. Several studies have demonstrated that PSC performance is strongly limited by the defect density in the absorber layer, particularly when it exceeds the critical range of 10^{15} - 10^{16} cm^{-3}. In particular, Wang *et al.* showed

through numerical simulations that increasing the defect density beyond 10^{16} cm^{-3}. leads to a significant reduction in the open-circuit voltage due to enhanced Shockley-Read-Hall recombination [26]. Overall, reducing the absorber defect density below the critical threshold of 10^{15} cm^{-3} effectively suppresses Shockley-Read-Hall recombination, increases carrier lifetime, and improves charge extraction toward the electrodes, thereby enhancing the performance of hybrid perovskite solar cells.

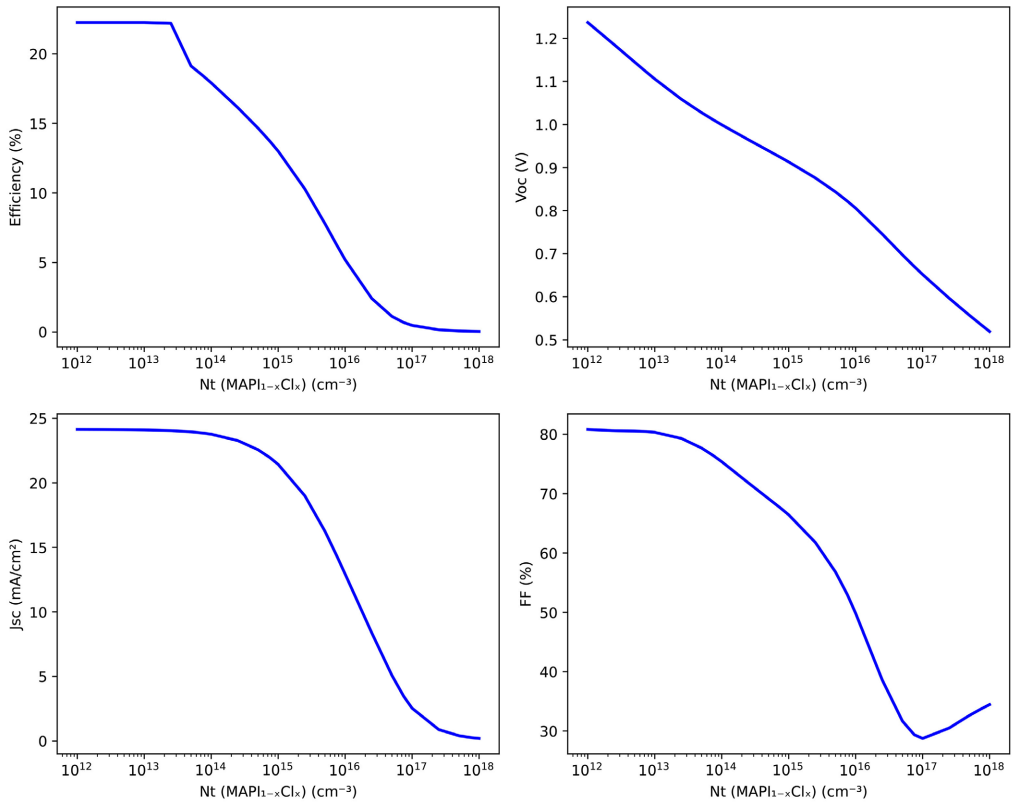

Figure 9. Influence of the defect density N_t in the $MAPI_{1-x}Cl_x$ absorber on the electrical parameters.

4. Conclusion

In this numerically based study, the SCAPS-1D simulation software was employed to investigate the impact of various hybrid electron transport layers (h-ETLs) on the performance of perovskite solar cells. The results demonstrate that among the different configurations examined, devices incorporating PCBM-SnS_2 and TiO_2-SnO_2 h-ETLs exhibit the best optoelectronic performance, particularly in terms of external quantum efficiency and overall power conversion efficiency. These superior performances are attributed to improved energy band alignment with the $MAPI_{1-x}Cl_x$ absorber layer, which promotes efficient electron extraction and reduces interfacial recombination losses. Based on these findings, the TiO_2-SnO_2 configuration was selected for further investigations due to its enhanced stability and superior electrical performance. A combined parametric study of the absorber and h-ETL thicknesses revealed that an optimal thickness of approximately 450

nm for the $MAPI_{1-x}Cl_x$ absorber and 30 nm for the TiO_2-SnO_2 layer yields the best overall device performance. Under these optimized conditions, a notable improvement in photovoltaic parameters was observed, including an increase in the short-circuit current density J_{SC} of approximately 4.19%, a controlled variation in the open-circuit voltage V_{OC} and an overall efficiency enhancement of about 1.23%. Furthermore, the analysis of defect density effects revealed that device performance is significantly more sensitive to defects in the absorber layer than in the electron transport layer. In particular, reducing the absorber defect density below the critical threshold of approximately 10^{15} cm^{-3} leads to a substantial suppression of non-radiative recombination mechanisms, resulting in marked improvements in open-circuit voltage, fill factor, and overall efficiency. These findings highlight the crucial role of parameters such as layer thickness and defect density in the design of next-generation high-efficiency perovskite solar cells and provide valuable guidelines for further performance optimization.

Conflicts of Interest

The authors declare no conflicts of interest regarding the publication of this paper.

References

[1] Kojima, A., Teshima, K., Shirai, Y. and Miyasaka, T. (2009) Organometal Halide Perovskites as Visible-Light Sensitizers for Photovoltaic Cells. *Journal of the American Chemical Society*, **131**, 6050-6051. https://doi.org/10.1021/ja809598r

[2] Green, M.A., Ho-Baillie, A. and Snaith, H.J. (2014) The Emergence of Perovskite Solar Cells. *Nature Photonics*, **8**, 506-514. https://doi.org/10.1038/nphoton.2014.134

[3] NREL (2024) Best Research-Cell Efficiencies Chart. National Renewable Energy Laboratory.

[4] Kim, H., Lee, C., Im, J., Lee, K., Moehl, T., Marchioro, A., *et al.* (2012) Lead Iodide Perovskite Sensitized All-Solid-State Submicron Thin Film Mesoscopic Solar Cell with Efficiency Exceeding 9%. *Scientific Reports*, **2**, Article No. 591. https://doi.org/10.1038/srep00591

[5] Niu, G., Guo, X. and Wang, L. (2015) Review of Recent Progress in Chemical Stability of Perovskite Solar Cells. *Journal of Materials Chemistry A*, **3**, 8970-8980. https://doi.org/10.1039/c4ta04994b

[6] Yang, J., Siempelkamp, B.D., Mosconi, E., De Angelis, F. and Kelly, T.L. (2017) Origin of Stability in Perovskite Solar Cells. *Energy & Environmental Science*, **10**, 143-151.

[7] Stranks, S.D., Eperon, G.E., Grancini, G., Menelaou, C., Alcocer, M.J.P., Leijtens, T., *et al.* (2013) Electron-Hole Diffusion Lengths Exceeding 1 Micrometer in an Organometal Trihalide Perovskite Absorber. *Science*, **342**, 341-344. https://doi.org/10.1126/science.1243982

[8] Mosconi, E., Amat, A., Nazeeruddin, M.K., Grätzel, M. and De Angelis, F. (2013) First-Principles Modeling of Mixed Halide Perovskites. *The Journal of Physical Chemistry Letters*, **4**, 3637-3642.

[9] Colella, S., Mosconi, E., Pellegrino, G., *et al.* (2013) Elusive Stoichiometry of Mixed Halide Perovskites. *Chemistry of Materials*, **25**, 4613-4618.

[10] Chen, Q., Zhou, H., Hong, Z., *et al.* (2016) Planar Heterojunction Perovskite Solar

Cells via Vapor-Assisted Solution Process. *Nature Communications*, **6**, Article No. 7269.

[11] Zhou, H., Chen, Q., Li, G., Luo, S., Song, T., Duan, H., *et al.* (2014) Interface Engineering of Highly Efficient Perovskite Solar Cells. *Science*, **345**, 542-546. https://doi.org/10.1126/science.1254050

[12] Leijtens, T., Eperon, G.E., Pathak, S., Abate, A., Lee, M.M. and Snaith, H.J. (2013) Overcoming Ultraviolet Light Instability of Perovskite Solar Cells. *Energy & Environmental Science*, **6**, 3472-3481.

[13] Ke, W. and Kanatzidis, M.G. (2019) Prospects for Low-Toxicity Lead-Free Perovskite Solar Cells. *Nature Communications*, **10**, Article No. 965. https://doi.org/10.1038/s41467-019-08918-3

[14] Li, X., Bi, D., Yi, C., *et al.* (2020) A Vacuum Flash-Assisted Solution Process for High-Efficiency Perovskite Solar Cells. *Advanced Functional Materials*, **30**, Article ID: 2000302.

[15] Kim, J., Lee, S.H., Lee, J.H. and Hong, K.H. (2021) The Role of Interfaces in Perovskite Solar Cells. *Energy & Environmental Science*, **14**, 2329-2340.

[16] Patil, P., Mann, D.S., Nakate, U.T., Hahn, Y., Kwon, S. and Na, S. (2020) Hybrid Interfacial ETL Engineering Using Pcbm-SnS_2 for High-Performance P-I-N Structured Planar Perovskite Solar Cells. *Chemical Engineering Journal*, **397**, Article ID: 125504. https://doi.org/10.1016/j.cej.2020.125504

[17] Li, S., Xing, Z., Wu, B., Chen, Z., Yao, Y., Tian, H., *et al.* (2020) Hybrid Fullerene-Based Electron Transport Layers Improving the Thermal Stability of Perovskite Solar Cells. *ACS Applied Materials & Interfaces*, **12**, 20733-20740. https://doi.org/10.1021/acsami.0c02119

[18] Noel, N.K., Stranks, S.D., Abate, A., *et al.* (2014) Enhanced Photoluminescence and Solar Cell Performance via Lewis Base Passivation. *Energy & Environmental Science*, **7**, 3061-3068.

[19] Wang, K., Liu, C., Du, P., Zheng, J. and Gong, X. (2019) Interface Engineering for Stable Perovskite Solar Cells. *Advanced Materials*, **31**, Article ID: 1902037.

[20] Yang, G., Tao, H., Qin, P., Ke, W. and Fang, G. (2016) SnS_2 as an Efficient Electron Transport Layer for Perovskite Solar Cells. *Journal of Materials Chemistry A*, **4**, 15949-15954.

[21] You, J., Hong, Z., Yang, Y., *et al.* (2014) Low-Temperature Solution-Processed Perovskite Solar Cells with High Efficiency. *Nature Nanotechnology*, **9**, 468-473.

[22] Burgelman, M., Nollet, P. and Degrave, S. (2000) Modelling Polycrystalline Semiconductor Solar Cells. *Thin Solid Films*, **361**, 527-532. https://doi.org/10.1016/s0040-6090(99)00825-1

[23] Burgelman, M., Decock, K., Niemegeers, A., Verschraegen, J. and Degrave, S. (2013) SCAPS Manual and Numerical Modeling of Solar Cells. *Solar Energy Materials and Solar Cells*, **110**, 103-110.

[24] Kanoun, A., Kanoun, M.B., Merad, A.E. and Goumri-Said, S. (2019) Toward Development of High-Performance Perovskite Solar Cells Based on $CH_3NH_3GeI_3$ Using Computational Approach. *Solar Energy*, **182**, 237-244. https://doi.org/10.1016/j.solener.2019.02.041

[25] Malla Hasan, H. and Onay, Ö. (2022) Investigation of Different Factors Affecting Perovskite Solar Cell Performance Using SCAPS. *European Journal of Engineering Science and Technology*, **5**, 20-38.

[26] Si, F., Tang, F., Xue, H. and Qi, R. (2016) Effects of Defect States on the Performance

of Perovskite Solar Cells. *Journal of Semiconductors*, **37**, Article ID: 072003. https://doi.org/10.1088/1674-4926/37/7/072003

[27] Tress, W. (2017) Metal Halide Perovskites as Mixed Ionic-Electronic Conductors. *Advanced Energy Materials*, **7**, Article ID: 1602358.